

Andreev rectifier

A nonlocal conductance signature of topological phase transitions

Rosdahl, T. O.; Vuik, A.; Kjaergaard, M.; Akhmerov, A. R.

DOI

[10.1103/PhysRevB.97.045421](https://doi.org/10.1103/PhysRevB.97.045421)

Publication date

2018

Document Version

Final published version

Published in

Physical Review B

Citation (APA)

Rosdahl, T. O., Vuik, A., Kjaergaard, M., & Akhmerov, A. R. (2018). Andreev rectifier: A nonlocal conductance signature of topological phase transitions. *Physical Review B*, *97*(4), Article 045421. <https://doi.org/10.1103/PhysRevB.97.045421>

Important note

To cite this publication, please use the final published version (if applicable). Please check the document version above.

Copyright

Other than for strictly personal use, it is not permitted to download, forward or distribute the text or part of it, without the consent of the author(s) and/or copyright holder(s), unless the work is under an open content license such as Creative Commons.

Takedown policy

Please contact us and provide details if you believe this document breaches copyrights. We will remove access to the work immediately and investigate your claim.

Andreev rectifier: A nonlocal conductance signature of topological phase transitionsT. Ö. Rosdahl,^{1,*} A. Vuik,^{1,†} M. Kjaergaard,^{2,3} and A. R. Akhmerov¹¹*Kavli Institute of Nanoscience, Delft University of Technology, P.O. Box 4056, 2600 GA Delft, Netherlands*²*Center for Quantum Devices and Station Q Copenhagen, Niels Bohr Institute, University of Copenhagen, Universitetsparken 5, 2100 Copenhagen, Denmark*³*Research Laboratory of Electronics, Massachusetts Institute of Technology, Cambridge, Massachusetts 02139, USA*

(Received 24 July 2017; revised manuscript received 29 November 2017; published 22 January 2018)

The proximity effect in hybrid superconductor-semiconductor structures, crucial for realizing Majorana edge modes, is complicated to control due to its dependence on many unknown microscopic parameters. In addition, defects can spoil the induced superconductivity locally in the proximitized system, which complicates measuring global properties with a local probe. We show how to use the nonlocal conductance between two spatially separated leads to probe three global properties of a proximitized system: the bulk superconducting gap, the induced gap, and the induced coherence length. Unlike local conductance spectroscopy, nonlocal conductance measurements distinguish between nontopological zero-energy modes localized around potential inhomogeneities, and true Majorana edge modes that emerge in the topological phase. In addition, we find that the nonlocal conductance is an odd function of bias at the topological phase transition, acting as a current rectifier in the low-bias limit. More generally, we identify conditions for crossed Andreev reflection to dominate the nonlocal conductance and show how to design a Cooper pair splitter in the open regime.

DOI: [10.1103/PhysRevB.97.045421](https://doi.org/10.1103/PhysRevB.97.045421)**I. INTRODUCTION**

The superconducting proximity effect occurs when a normal material (metal) is placed in contact with a superconductor. The resulting transfer of superconducting properties to the normal material [1,2] makes it possible to explore induced superconductivity in a range of materials that are not intrinsically superconducting, for example, in ferromagnetic metals [3–5] and in graphene [6–8]. Another recent application of the proximity effect is the creation of the Majorana quasiparticle [9–11], which is a candidate for the realization of topological quantum computation [12], and a focus of research efforts in recent years [13–15].

The proximity effect is due to the Andreev reflection of quasiparticles at the interface with the superconductor [2], which forms correlated electron-hole pairs that induce superconductivity in the normal material. This makes the proximity effect in real systems sensitive to microscopic interface properties, such as coupling strength, charge accumulation, and lattice mismatch [16,17]. Spatial inhomogeneities in the proximitized system, such as charge defects, may furthermore spoil the induced correlations locally. In a typical proximity setup, the superconductor proximitizes an extended region of a normal material, as shown in Fig. 1. A normal lead attached to one of the ends of the proximitized region probes the response to an applied voltage. When the coupling between the lead and the proximitized region is weak, the lead functions as a tunnel probe of the density of states in the latter. Since induced superconductivity may be inhomogeneous, and Andreev reflection happens locally, such an experiment only probes the

region in the direct vicinity of the normal lead, and not the overall properties of the proximitized region. For example, if the electrostatic potential is inhomogeneous, it may create accidental low-energy modes that are nearly indistinguishable from Majoranas [18–23].

We show how the *nonlocal* response between two spatially separated normal leads (see Fig. 1) may be used to probe both the bulk superconducting gap Δ and the induced gap Δ_{ind} , as well as the induced coherence length ξ . At subgap energies, quasiparticles propagate as evanescent waves with the decay length ξ in the proximitized system. This suppresses the nonlocal response with increasing separation L between the two normal leads [24–26]. Therefore, the length dependence of the nonlocal conductance measures when two ends of a proximitized system are effectively decoupled. When $L/\xi \gtrsim 1$, the nonlocal conductance is only possible in the energy window between the bulk superconducting gap Δ and the induced gap Δ_{ind} . The sensitivity to an induced gap allows one to use nonlocal conductance to distinguish between an induced gap closing and an Andreev level crossing at zero energy. In contrast, a local measurement may produce a similar result in both cases.

Two processes constitute the nonlocal response: direct electron transfer between the normal leads, and the crossed Andreev reflection (CAR) of an electron from one lead into a hole in the second lead [27,28]. Experimental [29–31] and theoretical [32–37] studies of CAR-dominated signals aim at producing a Cooper pair splitter [38–40], which has potential applications in quantum information processing. We show that applying a Zeeman field in the proximitized system creates wide regions in parameter space where CAR dominates the nonlocal response. Furthermore, we demonstrate how to obtain a CAR-dominated signal in the absence of a Zeeman field in the low-doping regime. Finally, we prove that at the topological

*torosdahl@gmail.com

†adriaanvuik@gmail.com

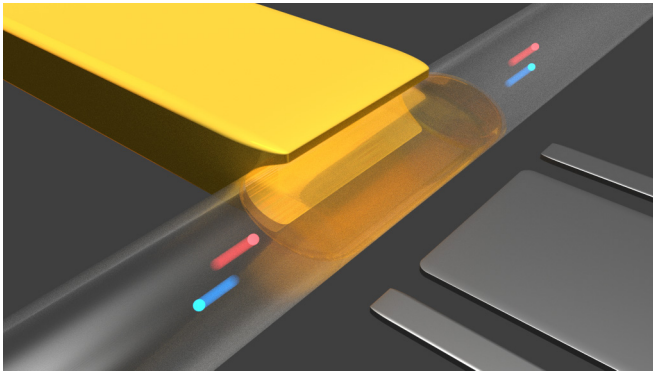


FIG. 1. A superconductor (yellow) proximitizes a semiconducting region (transparent) from the side. Narrow gates control the coupling of the proximitized scattering region with the leads, and a wider gate controls the chemical potential. An incoming electron from the left (red dot) undergoes either a local process, i.e., Andreev reflection into a hole (blue outgoing dot to the left) or normal reflection (not shown), or a nonlocal process (outgoing electron or hole to the right).

phase transition and with $L/\xi \gtrsim 1$, the nonlocal conductance is an approximately odd function of bias. This phenomenon only relies on particle-hole symmetry and hence manifests in both clean and disordered junctions. Therefore, a proximitized system coupled to normal leads acts as a rectifier of the applied voltage bias universally at the topological phase transition.

Our method is based on probing the bulk topological phase transition in Majorana devices, instead of the Majoranas themselves. Several other works propose different methods to probe the bulk instead of the edge states in one-dimensional topological superconductors. Quantized thermal conductance and electrical shot-noise measurements are predicted signatures of a bulk topological phase transition [41], and here we present a different route based on straightforward electrical conduction measurements in already available experimental systems. Further work predicts bulk signatures of a topological phase transition in the difference between the local Andreev conductances at each end of the proximitized region [42], or in the spin projection of bulk bands along the magnetic field direction [43]. In addition to probing the bulk topological phase transition, our proposed method allows one to probe a number of relevant physical parameters, and can be implemented in ongoing experiments, providing a technique to use in the hunt for Majoranas.

This paper is organized as follows. In Sec. II, we give an overview of our model and discuss the relevant energy and length scales. In Sec. III, we study how nonlocal conductance measures superconductor characteristics. We investigate the effects of a Zeeman field in homogeneous and inhomogeneous systems in Sec. IV. In Sec. V we consider the possible application of the proximitized system as a Cooper pair splitter. We finish with a summary and discussion of our results in Sec. VI.

II. MODEL AND PHYSICAL PICTURE

We consider a three-terminal device sketched in Fig. 2, with a normal central region of lateral length L and width W

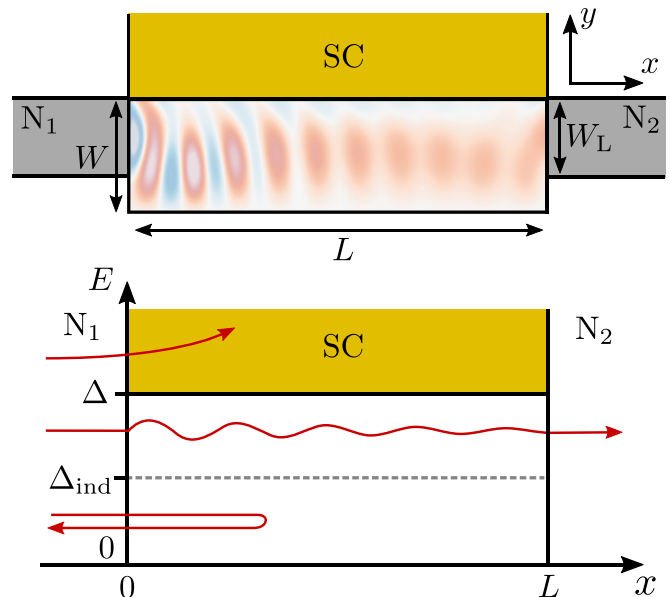


FIG. 2. Top: Schematic drawing of the device. A central region of length L and width W is connected from the sides to two normal leads N_1 (left) and N_2 (right) of width W_L , and from the top to one superconducting lead (SC) of width L . Superimposed is an example of the central region charge density, which oscillates between positive (red) and negative (blue). Bottom: Illustrations of possible scattering processes in energy space in the limit $L \gg \xi$. A quasiparticle, with energy below the induced gap, $|E| < \Delta_{\text{ind}}$, is reflected back into the source lead. A quasiparticle at $\Delta_{\text{ind}} < |E| < \Delta$ is transmitted to the right lead, either as an electron (normal transmission) or as a hole (crossed Andreev reflection). At energies exceeding the bulk gap, $|E| > \Delta$, the superconducting lead absorbs incoming quasiparticles.

separating two normal leads of width W_L . The device has a grounded superconducting lead of width L attached to the central region perpendicularly to the other two leads. This geometry models the proximity effect of a lateral superconductor on a slab of normal material, with normal leads probing the transport properties, and is therefore relevant both for heterostructures based on nanowires and quantum wells.

We model the hybrid system using the Bogoliubov–de Gennes Hamiltonian. For a semiconductor electron band with effective mass m^* and Rashba spin-orbit interaction (SOI) with strength α , it reads

$$H = \left(\frac{p_x^2 + p_y^2}{2m^*} - \mu \right) \tau_z + \Delta(y) \tau_x + \frac{\alpha}{\hbar} (p_y \sigma_x - p_x \sigma_y) \tau_z + E_Z(y) \sigma_x, \quad (1)$$

with $p_{x,y} = -i\hbar\partial_{x,y}$, μ the equilibrium chemical potential, and E_Z the Zeeman energy due to an in-plane magnetic field parallel to the interface between the central region and the superconductor. We assume a constant s -wave pairing potential that is nonzero only in the superconductor, $\Delta(y) = \Delta\theta(y - W)$ with $\theta(y)$ a step function, and choose Δ to be real since only one superconductor is present. We neglect the g factor in the superconductor since it is much smaller than in the adjacent semiconductor, such that $E_Z(y) = E_Z\theta(W - y)$, and our conclusions are not affected by this choice. The Pauli matrices σ_i

and τ_i act in spin and particle-hole space, respectively. The Hamiltonian acts on the spinor $\Psi = (\psi_{e\uparrow}, \psi_{e\downarrow}, \psi_{h\downarrow}, -\psi_{h\uparrow})$, which represents the electron (e) or hole (h) components of spin up (\uparrow) or down (\downarrow).

The superconductor induces an energy gap Δ_{ind} in the heterostructure. If $L \gg W$, the larger of two energy scales, namely, the bulk gap Δ and the Thouless energy E_{Th} , determines the magnitude of Δ_{ind} , with E_{Th} at low μ given by

$$E_{\text{Th}} = \gamma\delta, \quad \delta = \frac{\hbar^2\pi^2}{2m^*(2W)^2}, \quad (2)$$

where γ is the transparency of the interface with the superconductor and δ the level spacing. Our emphasis is on short and intermediate junctions, for which $E_{\text{Th}} \gg \Delta$ and $E_{\text{Th}} \lesssim \Delta$, respectively, such that $\Delta_{\text{ind}} \lesssim \Delta$. A brief review of normal-superconductor junctions in different limits and the relevant length and energy scales is given in the Appendix. We keep μ constant in the entire system but assume an anisotropic mass [44] in the superconductor with a component parallel to the interface, $m_{\parallel} \rightarrow \infty$. This approximation results in a transparent interface $\gamma = 1$ at normal incidence and at $E_Z = 0$, and is motivated by recent advances in the fabrication of proximitized systems with a high-quality superconductor-semiconductor interface [45,46].

We compute differential conductance using the scattering formalism. The scattering matrix relating all incident and outgoing modes in the normal leads of Fig. 2 is

$$S = \begin{bmatrix} S_{11} & S_{12} \\ S_{21} & S_{22} \end{bmatrix}, \quad S_{ij} = \begin{bmatrix} S_{ij}^{ee} & S_{ij}^{eh} \\ S_{ij}^{he} & S_{ij}^{hh} \end{bmatrix}. \quad (3)$$

Here, the $S_{ij}^{\alpha\beta}$ is the block of scattering amplitudes of incident particles of type β in lead j to particles of type α in lead i . Since quasiparticles may enter the superconducting lead for $|E| > \Delta$, the scattering matrix (3) is unitary only if $|E| < \Delta$. The zero-temperature differential conductance matrix equals [2,47]

$$G_{ij}(E) \equiv \frac{\partial I_i}{\partial V_j} = \frac{e^2}{h} (T_{ij}^{ee} - T_{ij}^{he} - \delta_{ij} N_i^e), \quad (4)$$

with I_i the current entering terminal i from the scattering region and V_j the voltage applied to the terminal j , and N_j^e the number of electron modes at energy E in terminal j . Finally the energy-dependent transmissions are

$$T_{ij}^{\alpha\beta} = \text{Tr}([S_{ij}^{\alpha\beta}]^\dagger S_{ij}^{\alpha\beta}). \quad (5)$$

The blocks of the conductance matrix involving the superconducting terminal are fixed by the condition that the sum of each row and column of the conductance matrix has to vanish. The finite-temperature conductance is a convolution of zero-temperature conductance with a derivative of the Fermi distribution function $f(E) = (1 + \exp(E/k_B T))^{-1}$:

$$G_{ij}(eV_j, T) = - \int_{-\infty}^{\infty} dE \frac{df(E - eV_j, T)}{dE} G_{ij}(E). \quad (6)$$

We discretize Hamiltonian (1) on a square lattice, and use KWANT [48] to numerically obtain the scattering matrix of Eq. (3) (see the Supplemental Material for the source code [49]). The resulting data are available in Ref. [50]. We obtain

ξ numerically by performing an eigendecomposition of the translation operator in the x direction for a translationally invariant system and computing the decay length of the slowest decaying mode at $E = 0$ [44,51]. We use the material parameters [52] $m^* = 0.023m_e$, $\alpha = 28$ meV nm, and unless otherwise specified $\Delta = 0.2$ meV, typical for an InAs two-dimensional electron gas with an epitaxial Al layer [45]. All transport calculations are done using $T = 30$ mK unless stated otherwise.

III. NONLOCAL CONDUCTANCE AS A MEASURE OF SUPERCONDUCTOR PROPERTIES

In the tunneling regime, the local conductance in a normal lead probes the density of states in the proximitized region, which is commonly used to measure the induced gap in experiment. However, such a measurement only probes the region near the tunnel probe and fails to give information about the density of states in the bulk of the proximitized region. The tunneling conductance is thus not a reliable probe of the entire proximitized region if the density of states varies spatially over the proximitized region, for example, due to an inhomogeneous geometry. As an illustration, Fig. 3 compares the local conductance G_{11} in the tunneling limit to the nonlocal conductance G_{21} in the open regime for a proximitized system that is inhomogeneous and in a magnetic field. Inhomogeneous systems are further treated in Sec. IV. The combination of an inhomogeneous system and broken time-reversal symmetry creates low-energy states localized near the junctions with the normal leads, which appear as peaks in the tunneling conductance. However, away from the junctions with the normal leads, the proximitized system remains close to fully gapped, the induced gap matching the energies at which the nonlocal conductance becomes finite in Fig. 3(b). Therefore, the nonlocal conductance is better than the local tunneling conductance as a probe for the induced gap in the bulk of the proximitized region. In the following, we

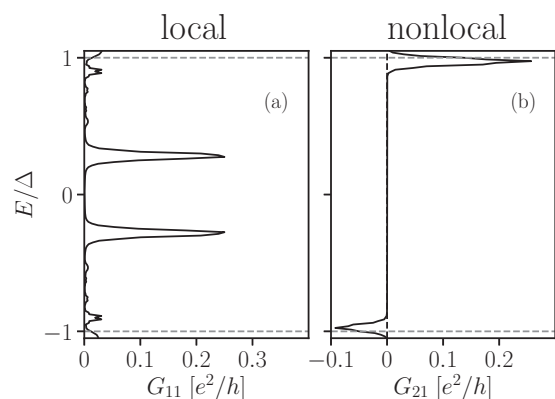


FIG. 3. Examples of (a) the local conductance in the tunneling regime and (b) the nonlocal conductance in the open regime of an inhomogeneous proximitized system with broken time-reversal symmetry. Localized low-energy states are present near the junctions with the normal leads. These manifest as peaks in the tunneling conductance, indicating $\Delta_{\text{ind}} \ll \Delta$. However, $\Delta_{\text{ind}} \approx \Delta$ still in the bulk of the proximitized system, with Δ_{ind} matching the energy at which the nonlocal conductance peaks.

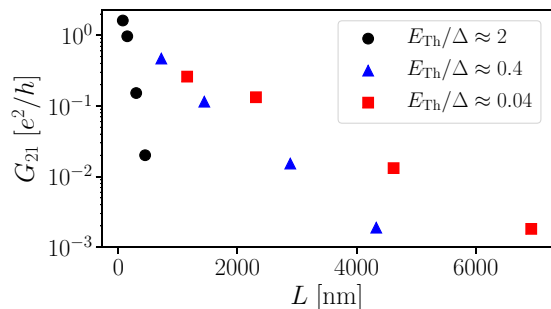


FIG. 4. Suppression of the nonlocal conductance G_{21} at zero bias $E = 0$ as a function of length for different ratios E_{Th}/Δ . For decreasing ratio E_{Th}/Δ , the induced coherence length ξ increases. This is reflected in the larger absolute length over which the nonlocal conductance is suppressed. Data points are taken from the $E = 0$ values of the nonlocal conductance presented in Fig. 5.

describe three ways in which the nonlocal conductance probes induced superconductivity.

First of all, the nonlocal conductance measures the induced decay length ξ in the bulk of the proximitized region between the two normal leads. To understand this, consider a nonlocal process at a subgap energy $|E| < \Delta_{ind}$. An electron injected from a normal lead must propagate as an evanescent wave $\propto e^{-x/\xi + ikx}$ through the gapped central region to the second normal lead, with ξ the decay length. Accordingly, as shown in Fig. 4, increasing L suppresses the nonlocal conductance at $E = 0$ exponentially [28,38]. Therefore, the suppression of the nonlocal conductance with increasing length L at $E = 0$ is a measure of the induced decay length ξ .

Furthermore, the nonlocal conductance measures the bulk gap Δ of the superconductor. Increasing L also suppresses the nonlocal conductance G_{21} for $|E| > \Delta$, as the right-hand column of Fig. 5 shows. For energies above the bulk superconducting gap Δ , the superconductor increasingly absorbs quasiparticles when the length is increased, and suppresses the nonlocal conductance to zero when $L \gg \xi$. Hence, the energy above which nonlocal conductance is suppressed at large lengths is a measure of Δ .

In addition, the nonlocal conductance measures the induced superconducting gap Δ_{ind} . When $L \gtrsim \xi$, the nonlocal conductance is suppressed at $E = 0$ but grows in a convex shape with E and peaks around $|E| \approx \Delta_{ind}$, as shown in the right-hand column of Fig. 5. This is due to a divergence in ξ , since the system is no longer gapped. To illustrate the correspondence between the nonlocal conductance and Δ_{ind} , the left-hand column of Fig. 5 shows the dispersions of the corresponding proximitized systems that have the normal leads removed and are translationally invariant along the x direction, such that $k = p_x/\hbar$ is conserved. Because the system is not gapped for $|E| > \Delta_{ind}$, G_{21} is generally nonzero at these energies. Note that aside from occasional dips to negative G_{21} , direct electron transfer dominates the nonlocal response (we investigate this in more detail in Sec. V).

The presence of finite nonlocal conductance in the energy range $\Delta_{ind} < |E| < \Delta$ depends only on density of states of the proximitized system and therefore still holds in the presence of disorder. In Fig. 6, we show the effects of disorder on the

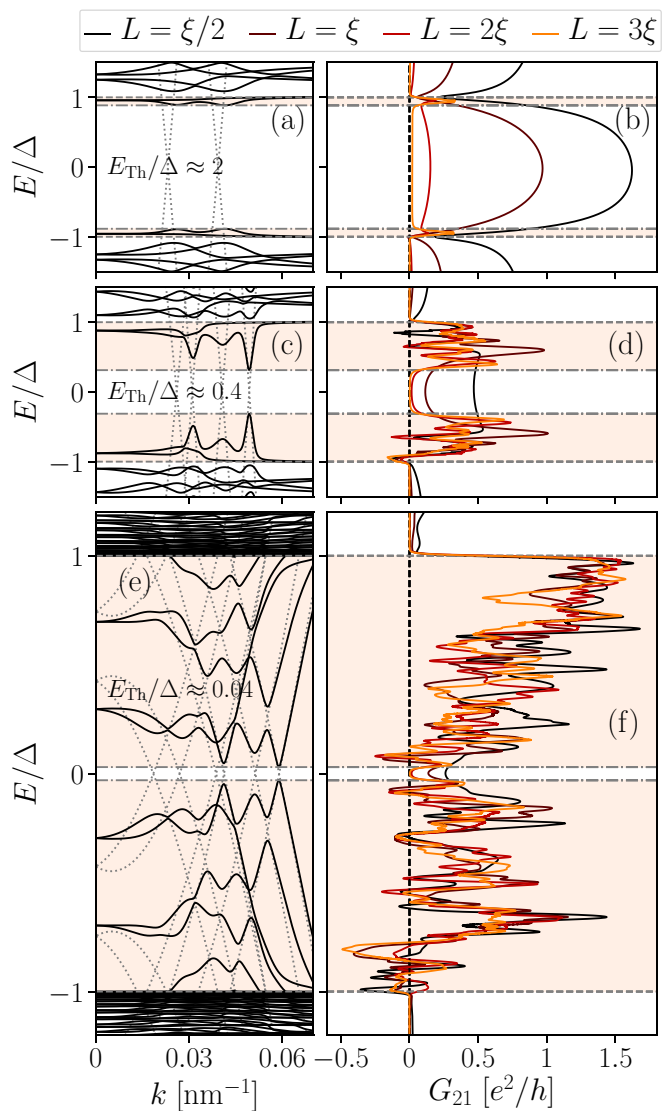


FIG. 5. (a, c, e) Dispersions of proximitized systems that are translationally invariant along x , and (b, d, f) nonlocal conductance $G_{21}(E)$ of corresponding junctions of finite length. The latter is shown as the separation L between the two normal leads is varied, with brightening colors from black to orange denoting $L = \xi/2, \xi, 2\xi$, and 3ξ , respectively. The ratio E_{Th}/Δ becomes smaller from top to bottom, such that Δ_{ind} shrinks (dash-dotted lines). For $L \gg \xi$, the nonlocal conductance is suppressed if $|E| < \Delta_{ind}$ and finite only for $\Delta_{ind} < |E| < \Delta$ (colored region). The solid lines in the dispersion relations show the dispersion of the normal-superconductor system, while the dotted lines show the electron and hole dispersion of the normal channel only, with the superconductor removed. We have $W = 100$ nm in (a) and (b), $W = 200$ nm in (c)–(f), and $W_L = 100$ nm always in the right column; $\mu = 3$ meV, $\Delta = 0.2$ meV, and $T = 30$ mK in the top and middle rows, but $\mu = 4.2$ meV, $\Delta = 2$ meV, and $T = 100$ mK in the bottom row. Dispersions are even in k .

transport signatures of Δ and Δ_{ind} for short and intermediate junctions when $L \gtrsim \xi$. We include on-site disorder in the central region and vary the elastic mean free path l_e from $l_e = L$ to $l_e = 0.1L$ [53]. Even in the presence of disorder, all of the aforementioned qualities are still apparent in the nonlocal conductance [Figs. 6(a) and 6(b)], namely, suppression for

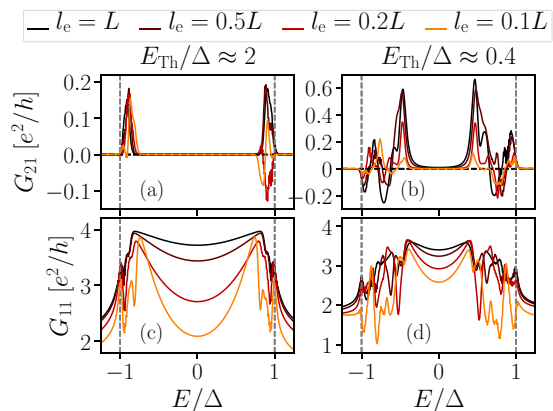


FIG. 6. (a, b) Nonlocal and (c, d) local conductance G_{21} and G_{11} of short (left-hand column) and intermediate (right-hand column) junctions with $L \gtrsim \xi$, to decouple the two normal leads at $|E| < \Delta_{\text{ind}}$. The mean free path varies between curves, with brightening colors from black to light orange denoting $l_e = L, L/2, L/5$, and $L/10$, respectively. Even in the presence of disorder, signatures of Δ_{ind} and Δ are visible in the nonlocal conductance. The local conductance is Andreev enhanced at subgap energies, but normal reflection becomes more prominent with increasing disorder. We have $W = 100$ nm and $L = 8\xi$ in (a) and (c), $W = 200$ nm and $L = 2\xi$ in (b) and (d), and $W_L = 100$ nm always, with $\mu = 3$ meV.

$|E| < \Delta_{\text{ind}}$, a finite signal for $\Delta_{\text{ind}} < |E| < \Delta$, and vanishing conductance for $|E| > \Delta$. Therefore, the nonlocal conductance remains a reliable probe of induced superconductivity even in the presence of disorder.

Lastly, in the absence of extended potential inhomogeneities, Δ and Δ_{ind} may also be inferred from the local conductance G_{11} in the open regime. As Figs. 6(c) and 6(d) show, $G_{11} \lesssim 4e^2/h$ in the ballistic case $l_e = L$ for $|E| < \Delta_{\text{ind}}$, which indicates that Andreev reflection is the dominant local process. This is the expected behavior for a normal-superconductor junction with high interface transparency [2,45] and is consistent with our results. Reducing the mean free path makes normal reflection more likely and hence lowers G_{11} , similar to an ideal normal-superconductor junction with a reduced interface transparency. Here, comparing G_{11} and G_{21} shows that Δ_{ind} and Δ may also be inferred from the local conductance, because it changes smoothly with bias only outside the interval $\Delta_{\text{ind}} < |E| < \Delta$. However, the signatures are clearer in G_{21} , where it is a transition between finite and vanishing conductance that indicates the gaps. Furthermore, the induced gap observed in the local and nonlocal conductances coincide here only due to the absence of extended potential inhomogeneities. For the case of an inhomogeneous geometry as in Fig. 3, only the nonlocal conductance correctly measures Δ_{ind} in the bulk of the proximitized system.

IV. ANDREEV RECTIFIER AT THE TOPOLOGICAL PHASE TRANSITION

A. Andreev rectification as a measure of the topological phase

In order to study nonlocal conductance at the topological phase transition, we apply an in-plane Zeeman field along the x direction of the proximitized system. Figure 7 shows

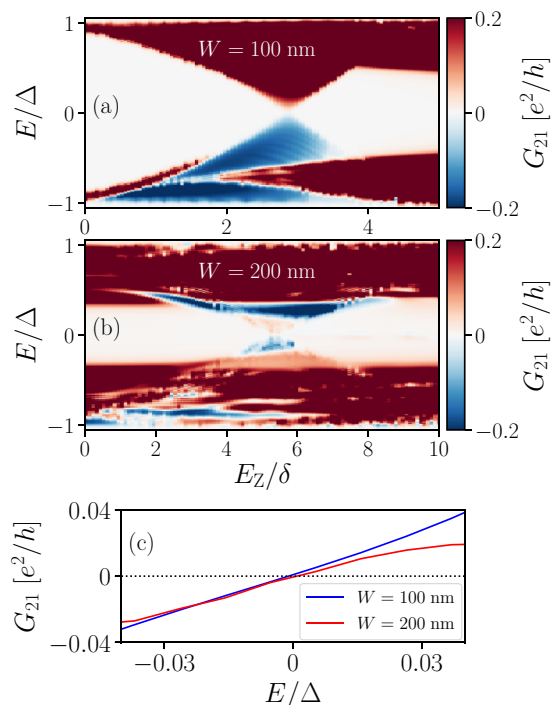


FIG. 7. Nonlocal conductance G_{21} in the single-mode regime as a function of E and E_Z in the absence of disorder (a) $W = 100$ nm and (b) $W = 200$ nm. The Zeeman field closes the induced gap and the system undergoes a topological phase transition. At the transition, G_{21} vanishes and changes sign as a function of bias. There are prominent regions where the nonlocal conductance is negative, i.e., where CAR dominates. The color scale is saturated for clarity. (c) Line cuts of G_{21} as a function of bias at the topological phase transition, taken at $E_Z \approx 2.9\delta$ for $W = 100$ nm and $E_Z \approx 5.4\delta$ for $W = 200$ nm, showing that the nonlocal conductance is an approximately odd function of bias.

the nonlocal conductance G_{21} as a function of bias E and Zeeman energy E_Z , for short and intermediate junctions in Figs. 7(a) and 7(b) with $L = 10\xi$ and $L = 3\xi$, respectively, such that the two normal leads are well decoupled, and the nonlocal conductance is exponentially suppressed at subgap energies. Increasing the magnetic field closes the induced gap and the system is driven into a topological phase. The line cuts of Fig. 7(c), taken at the critical magnetic field $E_Z = E_Z^c$, show that at the topological phase transition the nonlocal conductance is a linear function of energy, $G_{21}(E) \propto E$ around $E = 0$. At the topological phase transition, the current $I \propto V^2$ with V the voltage bias, and the system functions as a current rectifier due to crossed Andreev reflection.

This Andreev rectifier manifests due to the topology and symmetry of the proximitized system. The system only has particle-hole symmetry and is therefore in class D [54,55]. Expanding $G_{21}(E, E_Z) = c_0(E_Z) + c_1(E_Z)E + O(E^2)$ around $E = 0$, the exponential suppression of G_{21} at subgap energies means that the coefficients c_0 and c_1 are exponentially suppressed at magnetic fields before the topological phase transition. In class D systems, if G_{21} is exponentially suppressed at subgap energies, it is guaranteed to remain exponentially suppressed across the topological phase transition [41,56]. At the critical magnetic field $E_Z = E_Z^c$, $G_{21}(E = 0, E_Z^c) = c_0(E_Z^c)$

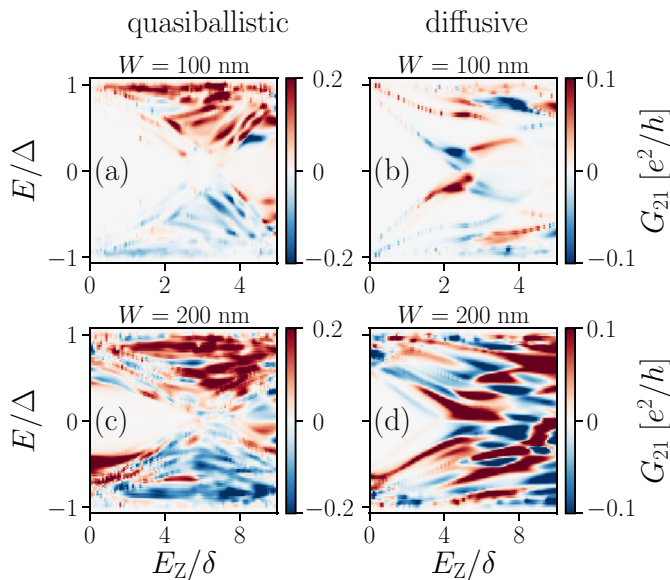


FIG. 8. The nonlocal conductance G_{21} as a function of E and E_Z for a proximitized system that is quasiballistic [(a), (c) with $\mu = 3$ meV] and diffusive [(b), (d) with $\mu = 16$ meV]. For the diffusive junction, the leads are gated into the single-mode regime using quantum point contacts at the junctions with the channel. Top and bottom rows present results for $W = 100$ and 200 nm, respectively. For the quasiballistic junction, $L/\xi = 8$ and 2 for $W = 100$ and 200 nm, respectively, and the mean free path is $l_e = 0.2L$ in each case. In the diffusive system, we have $l_e = 0.2W$ and $L/\tilde{\xi} = 5$ and 2 for the widths, respectively, where $\tilde{\xi} = \sqrt{l_e \xi}$. The color scale is saturated in both cases for clarity.

is therefore also exponentially suppressed. However, the system is gapless at the topological phase transition, such that G_{21} is generally finite at any nonzero E , and $c_1(E_Z^c)$ thus is not exponentially suppressed. At the topological phase transition, we therefore have $G_{21} \propto E$ in the limit $E \rightarrow 0$, where higher-order contributions are negligible. Consequently, rectifying behavior in the nonlocal conductance is an indication of a topological phase transition. This makes the nonlocal conductance not only a probe of the bulk properties of induced superconductivity as discussed in Sec. III, but also makes it selectively sensitive to topological phase transitions.

The rectifying behavior $G_{21} \propto E$ at the topological phase transition in Fig. 7 is grounded in the symmetry classification of the channel. As a result, we expect it to be robust to the presence of on-site disorder, so long as it does not alter the symmetry class. Figure 8 shows G_{21} as a function of E and E_Z for systems with the same widths as in Fig. 7. In the left-hand column, parameters are chosen identical to those in Fig. 7, with the addition of on-site disorder to give an elastic mean free path $l_e = 0.2L$ [53], bringing the systems well into the quasiballistic regime. In the right-hand column of Fig. 8, we investigate G_{21} when the central region is in the diffusive limit, with $l_e = 0.2W$. The widths are the same as in the quasiballistic (and clean) case, but μ is increased such that several modes are active. We gate the leads into the single-mode regime using quantum point contacts at the junctions with the scattering region. In each case we pick $L \gtrsim \tilde{\xi}$, since in the diffusive limit $\tilde{\xi} = \sqrt{l_e \xi}$ governs the range

of the coupling between the two normal terminals at subgap energies [57]. In both quasiballistic and diffusive cases, G_{21} remains an approximately odd function of E around the gap closing, and the proximitized system therefore acts as a rectifier even in the presence of disorder.

B. Distinguishing the topological phase transition in spatially inhomogeneous devices

Several works [18–23] discuss the emergence of zero-energy modes in the trivial phase of a hybrid semiconductor-superconductor device with an extended, spatially inhomogeneous potential. Local conductance measurements do not distinguish between these modes and well-separated Majorana modes at the end points of the proximitized region in the topological phase, since both give rise to zero-bias conductance features.

To study this problem, we include an extended inhomogeneous potential,

$$\phi(x, y) = V_0 \exp\left[-\frac{1}{2}\left(\frac{x-x_0}{d_x}\right)^2\right] \exp\left[-\frac{1}{2}\left(\frac{y-y_0}{d_y}\right)^2\right], \quad (7)$$

in the setup shown in Fig. 2, with V_0 the potential amplitude, x_0 and y_0 the coordinates of the potential center, and d_x and d_y parameters to control the smoothness in the x and y directions, respectively. We compare conductance for an amplitude $V_0 = -4.5$ mV to conductance in a homogeneous system $V_0 = 0$ V. We calculate the local conductance in the tunneling regime, with tunnel barriers at both wire ends $x = 0$ and $x = L$, and the nonlocal conductance in the open regime, with the system length fixed to $L = 8\xi$ and the width to $W = 100$ nm. To confirm that such a spatially inhomogeneous system can indeed exhibit trivial zero-energy modes, we calculate the low-energy spectrum of our system when decoupled from the leads, forming a closed superconductor-semiconductor system. The phase transition is computed from the absolute value of the determinant of the reflection matrix in the open system at $E = 0$, with $|\det(r)| = 1$ everywhere for $L \gg \xi$, except at the phase transition, where it drops to zero [58]. Figure 9(a) shows the spectrum as a function of E_Z in the homogeneous case ($V_0 = 0$), Fig. 9(b) for the inhomogeneous case ($V_0 = -4.5$ mV). While in the first case the closing of the induced superconducting gap coincides with the topological phase transition, in the second case an extended topologically trivial region exists with states around zero energy (yellow region).

Comparing the local conductance with and without an inhomogeneous potential, we find that zero-energy modes appear regardless of whether they are topological or trivial. Figures 9(c) and 9(d) show the local response as a function of bias and Zeeman energy when leads are connected to the central region via tunnel barriers. Since the system is ballistic and long ($L \gg \xi$), the local conductance agrees well with the spectra presented in Figs. 9(a) and 9(b). Accordingly, the local conductance in Fig. 9(d) for $V_0 = -4.5$ mV shows zero-energy modes in the topologically trivial regime. Therefore, a gap closing and the emergence of zero-energy modes in the local

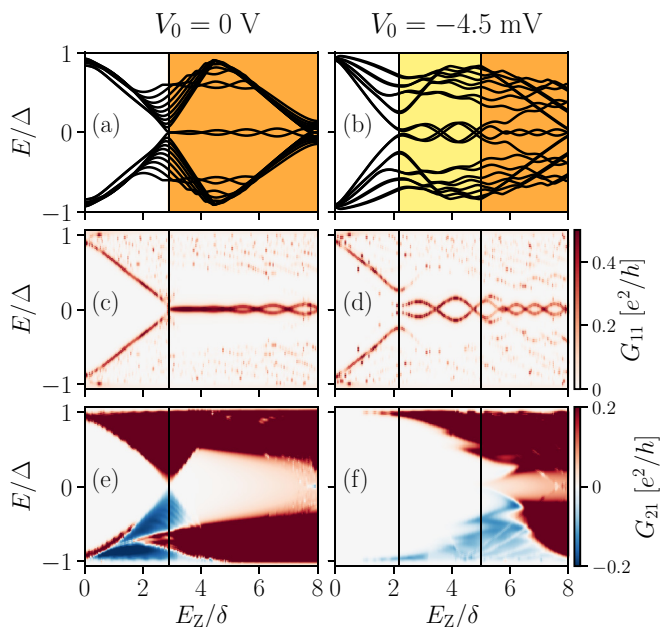


FIG. 9. (a, b) Spectrum, (c, d) local conductance G_{11} , and (e, f) nonlocal conductance G_{21} of a system without potential variations (left-hand column) and a system with a long-range Gaussian potential of amplitude $V_0 = -4.5$ mV (right-hand column). The orange region in (a) and (b) denotes the topological phase, and yellow the trivial phase with a state around zero energy. G_{11} is calculated in the presence of two tunnel barriers at both wire ends, G_{21} in the single-mode regime. The color scale is saturated for clarity. For the potential inhomogeneity, we set $V_0 = -4.5$ meV, $x_0 = L/2$, $y_0 = W/2$, $d_x = L/5$, and $d_y = 2W/3$.

conductance is not a sufficient sign of a topological phase transition.

On the other hand, nonlocal conductance has a much clearer signature of the topological transition than the local conductance. To demonstrate this, in Figs. 9(e) and 9(f) we show the nonlocal conductance as a function of bias and Zeeman energy. For both the homogeneous case and the inhomogeneous case, the appearance of nonlocal conductance around $E = 0$ coincides with the change of the topological invariant. In other words, the appearance of finite nonlocal conductance around $E = 0$ implies a global closing of the induced gap. Additionally, the nonlocal conductance shows rectifying behavior around $E = 0$ at the gap closing. These two features of the nonlocal conductance are strong evidence of a topological phase transition. Therefore, due to its insensitivity to spatial inhomogeneities in the potential and the additional feature of Andreev rectification, nonlocal conductance is a more reliable measure of a topological phase transition.

V. COOPER PAIR SPLITTER

A negative nonlocal conductance, dominated by CAR, is of fundamental interest, since the proximitized system then functions as a Cooper pair splitter [38–40,59,60]. In Sec. III, we observed that the nonlocal conductance in clean systems at zero magnetic field is generally positive, and a CAR-dominated signal ($G_{21} < 0$) is rare. The reason for this is shown

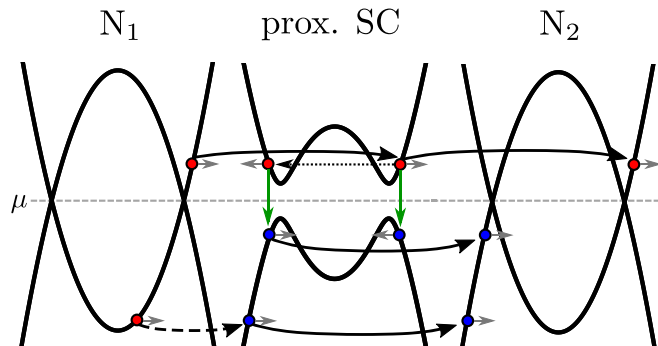


FIG. 10. Schematic of the quasiparticle transport properties from the normal lead N_1 to the lead N_2 through the proximitized region. Quasiparticles transferring to a neighboring region (solid black arrows) predominantly preserve the quasiparticle type: electronlike (red dots) or holelike (blue dots). Andreev reflection (green vertical arrows) changes the quasiparticle type and the direction of propagation (grey arrows). Disorder scattering (black dotted arrow) changes the propagation direction. Finally, if no quasiparticles of the same type are available, quasiparticle transmission between regions may also result in the change of the quasiparticle type (black dashed arrow).

schematically in Fig. 10: an electron entering the proximitized region usually converts into an electronlike quasiparticle. Andreev reflection changes both the quasiparticle charge and velocity, so that the resulting holelike quasiparticle returns to the source. Therefore, under normal circumstances Andreev reflection alone is insufficient to generate a negative nonlocal current.

Despite that G_{21} stays predominantly positive in clean systems, in Sec. IV we found that a magnetic field can make the nonlocal conductance negative in large regions of parameter space. We identify these regions with the presence of only holelike bands in the proximitized region at the relevant energy, as shown in Fig. 10. If only holelike states are present in the proximitized region, the incoming electron may only convert into a right-moving holelike quasiparticle, which in turn converts predominantly into a hole when exiting the proximitized region. To confirm this argument, we compare the energy ranges where only holelike quasiparticles are present with the regions of negative G_{21} . Our results are shown in Fig. 11, and they exhibit a very good agreement. Since the only required property to get a negative nonlocal conductance is a holelike dispersion relation, this phenomenon does not require SOI, or even a Zeeman field. Indeed, our calculations (not shown here) reveal that it is possible to extend the energy ranges over which CAR dominates by filtering the nonlocal conductance by spin, e.g., by using magnetically polarized contacts [27].

It is possible to systematically obtain a negative nonlocal conductance in the low-doping regime without using a Zeeman field if $\Delta > \Delta_{\text{ind}}$. This is shown in Figs. 11(c) and 11(d), where we have also neglected SOI for simplicity. By choosing μ comparable to the band offset of the lowest mode in the proximitized channel, at negative energies we obtain an energy range in which the band structure is only holelike [Fig. 11(c)]. However, the small μ implies that no electron modes are active in the normal leads in this energy range. To observe negative nonlocal conductance here, it is therefore necessary

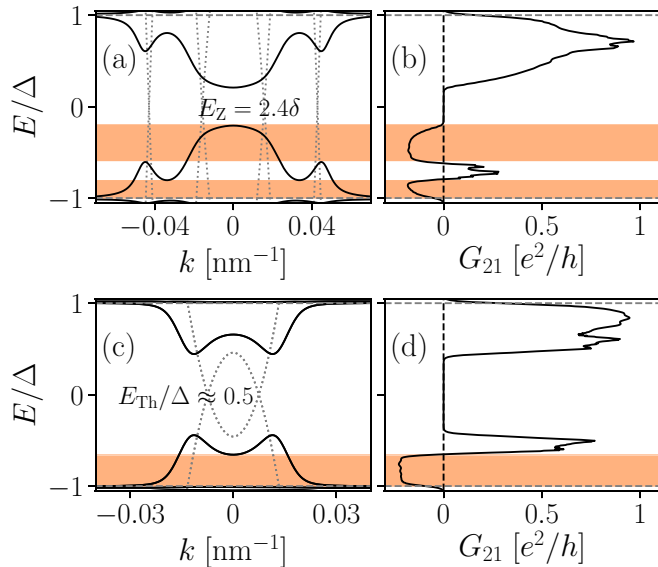


FIG. 11. Dispersions (left-hand column) and nonlocal conductance with $L \gg \xi$ (right-hand column) of proximitized channels of width (a, b) $W = 100$ nm and (c, d) $W = 200$ nm. Dotted lines show the electron and hole dispersions of the channels with the superconductor removed. In both cases, the induced gap is smaller than Δ , due to a Zeeman field in (a) and due to $E_{\text{Th}} \lesssim \Delta$ in (c). There are energy ranges in which only holelike bands are present, and these correspond to regions of negative G_{21} . Here, (c) is in a low-doping regime $\mu = 0.5$ meV, such that electron modes are absent for $E/\Delta \lesssim -0.5$, producing the holelike dispersion. As a result, a larger chemical potential $\mu = 0.8$ meV is needed in the normal leads to observe $G_{21} < 0$ at the corresponding energies in (d). In (a) and (b), we have $\mu = 3$ meV.

to have a larger chemical potential in the normal leads than in the proximitized region, which ensures the presence of propagating electron modes at the relevant energies. Doing so, we indeed observe a negative nonlocal conductance in the expected energy range of Fig. 11(d).

Disorder provides an alternative mechanism to obtain negative nonlocal conductance. Unlike direct electron transfer, which generally conserves the sign of quasiparticle momentum, CAR often requires a sign change of the quasiparticle momentum. Since disorder breaks momentum conservation, the probabilities of CAR and direct electron transfer become comparable once the system length exceeds the mean free path, and CAR is thus more prominent than in a clean system. Indeed, as shown in Fig. 8, in disordered systems the nonlocal conductance becomes positive or negative with approximately equal probability.

VI. SUMMARY AND OUTLOOK

The standard experimental tool for probing induced superconductivity in a Majorana device is a tunneling conductance measurement using an attached normal lead. While this approach detects the density of states, its usefulness is limited because it cannot distinguish the properties in close vicinity of the lead from the properties of the bulk system. We studied how the *nonlocal* conductance between two spatially separated

normal leads attached to the proximitized region overcomes this limitation. We find that the nonlocal conductance is selectively sensitive to the bulk properties of a proximity superconductor, which allows to directly measure the induced and the bulk superconducting gaps as well as the induced coherence length of the proximitized region. While we focused on the quasi-one-dimensional systems suitable for the creation of Majorana states, our conclusions are applicable to general proximity superconductors, including two-dimensional materials like graphene covered by a bulk superconductor.

When the probability of CAR is larger than that of electron transmission, the nonlocal conductance turns negative. While this does not happen normally, we identified conditions that allow CAR to dominate. This may happen due to disorder, which breaks the relation between quasiparticle charge, velocity, and momentum and makes the nonlocal conductance zero on average. We identified another, systematic way of obtaining dominant CAR by ensuring that the only available states in the proximitized region are holelike. A special case of this behavior is the vicinity of the topological phase transition, where the nonlocal conductance becomes proportional to voltage, resulting in a linear relation between the differential conductance and voltage or, in other words, a positive nonlocal current regardless of the sign of the voltage. This behavior is specific to topological phase transitions, and we showed how it can be used to distinguish accidental low-energy states from Majorana tunneling experiments identified in Refs. [19–23].

Our setup can be used with trivial adjustments to probe the properties of Josephson junctions, proposed as a promising alternative platform for the creation of Majorana states [54,55]. Further work could investigate interaction effects on the nonlocal response [61]. An alternative promising avenue of follow-up work is to consider a multiterminal generalization of a nonlocal setup in order to combine local and global sensitivity within the same device. In Fig. 12 we show a possible experimental realization of such a multiterminal device, where the effective length can be adjusted with gates. Finally, our results regarding control of the CAR dominance can be used to design devices with a large electron-hole conversion efficiency.

ACKNOWLEDGMENTS

We thank D. Sticlet, M. P. Nowak, and M. Wimmer for fruitful discussions. This work was supported by ERC Starting Grant No. 638760, the Netherlands Organisation for Scientific Research (NWO/OCW), as part of the Frontiers of Nanoscience program and the US Office of Naval Research. M.K. gratefully acknowledges support from the Carlsberg Foundation.

APPENDIX: SHORT, INTERMEDIATE, AND LONG JUNCTION LIMITS FOR HYBRID STRUCTURES

In this Appendix, we briefly discuss the subgap spectral characteristics of normal-superconductor junctions in different limits, using heuristic arguments to highlight the essential physics. For a more rigorous study, we refer the interested reader to, e.g., Refs. [62–66]. Consider a quasi-one-dimensional channel of length $L \rightarrow \infty$ that consists of

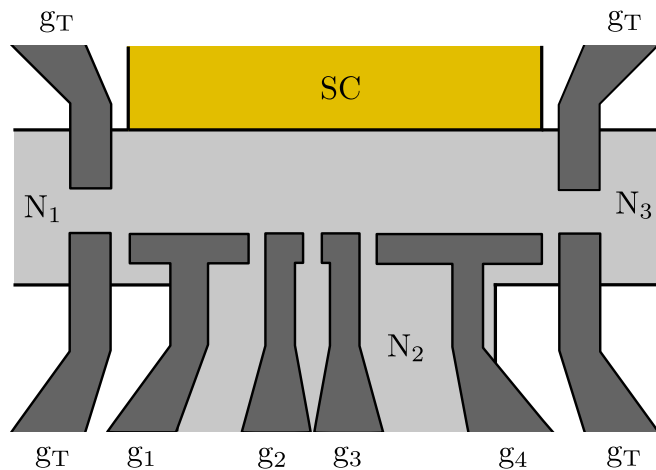


FIG. 12. A possible experimental realization of a multiterminal proximitized device suited for nonlocal conductance measurements. Electrostatic gates g_i , $i \in \{1,2,3,4\}$, pattern out a quasi-one-dimensional region in a two-dimensional electron gas, which is proximitized from the side by a superconductor. Gates g_T create tunnel barriers at the end points of the proximitized region. Changing the potentials applied to the gates allows for changing the effective device length.

a junction between a normal part of width W and a superconductor of width $W_{sc} \gg W$. The Hamiltonian is the same as in Eq. (1), but with $p_x \rightarrow \hbar k$ and as before $\Delta \neq 0$ only in the superconductor. Furthermore, we consider only $E_Z = 0$ and neglect SOI ($\alpha = 0$) and disorder for simplicity.

The hybrid structure generally has an energy gap Δ_{ind} , the size of which is determined by two competing energy scales, namely, the bulk gap Δ and the Thouless energy $E_{Th} \approx \hbar/\tau$, with τ the quasiparticle dwell time in the normal part of the junction. A short junction has $\Delta \ll E_{Th}$ and a long junction $\Delta \gg E_{Th}$, while $\Delta \gtrsim E_{Th}$ for an intermediate junction. Alternatively, these conditions are expressed in terms of W and the BCS coherence length $\xi_0 = \hbar v_F/\Delta$, where v_F is the Fermi velocity. For a quasiparticle incident perpendicularly from the normal part to the interface with the superconductor and assuming perfect interface transparency, we have $\tau \propto W/v_F$ and thus $E_{Th} \propto \hbar v_F/W$. The conditions for short, intermediate, and long junctions then become $W \ll \xi_0$, $W \gtrsim \xi_0$, and $W \gg \xi_0$, respectively. In the short-junction limit, we have $\Delta_{ind} \approx \Delta$, while for long and intermediate junctions $\Delta_{ind} \propto E_{Th}$.

We now derive a lower bound for E_{Th} in terms of the level spacing δ in the normal part of the junction. A quasiparticle exiting the superconductor has the dwell time $\tau \propto 2W/\gamma v_{\perp}(k)$ in the normal part. Here, $v_{\perp}(k) = \hbar k_{\perp}(k)/m^*$ and $k_{\perp} = \sqrt{k_F^2 - k^2}$ are respectively the velocity and momentum projections perpendicular to the interface with the superconductor at the parallel momentum k , with k_F the Fermi momentum, and $2W$ is the distance the quasiparticle travels before colliding with the superconductor again. The dwell time scales inversely with the transparency γ of the interface between the normal part and the superconductor. In practice, the transparency is determined by interface properties, such as the presence of a barrier or velocity mismatch, which we parametrize with $0 \leq \gamma \leq 1$ for simplicity. We thus obtain

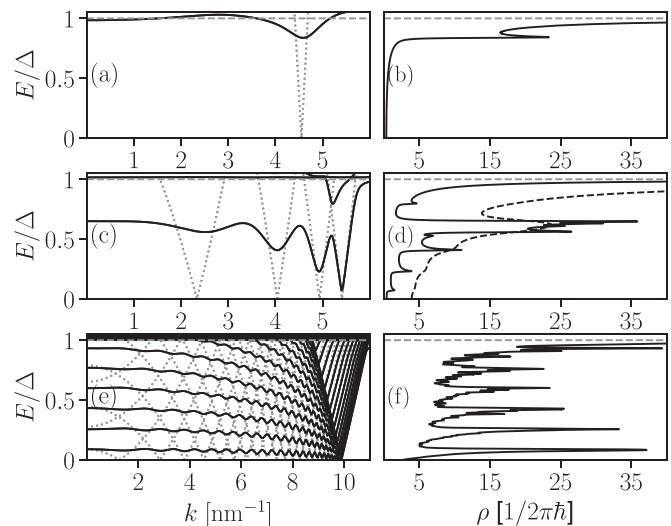


FIG. 13. Dispersion (left-hand column) and density of states (right-hand column) of a quasi-one-dimensional normal-superconductor junction in different regimes: a short junction (top), an intermediate junction (middle), and a long junction (bottom). In the left-hand column, the dotted curves show the electron and hole dispersions of the corresponding normal channel with the superconductor removed. In all cases, a small broadening $\Gamma \ll \Delta$ has been added to the density of states. For the intermediate junction (d), the density of states with larger broadening is also shown (dashed curve). The curves are symmetric under $(k, E) \rightarrow (\pm k, \pm E)$.

$E_{Th}(k) \propto \gamma \hbar^2 \sqrt{k_F^2 - k^2}/2m^*W$. Observe that E_{Th} decreases with k and tends to vanish as $k \rightarrow k_F$ since then $v_{\perp} \rightarrow 0$. However, v_{\perp} is bounded from below in a finite geometry by the momentum uncertainty associated with the band offset, which corresponds to the velocity $dv_{\perp} \approx \hbar\pi/m^*W$ in a square-well approximation. Using $v_{\perp} = dv_{\perp}$ gives the lower bound for the Thouless energy $E_{Th} \propto \gamma \hbar^2 \pi/2m^*W^2$. The preceding discussion implies that in the absence of magnetic fields, the gap in the spectrum of such a junction decreases with momentum to a minimum $\propto 1/m^*W^2$ at $k = k_F$ (see left-hand column of Fig. 13). Since Δ_{ind} is the energy of the lowest Andreev bound state in the junction, we define

$$E_{Th} = \gamma \delta, \quad \delta = \frac{\hbar^2 \pi^2}{2m^*(2W)^2}, \quad (\text{A1})$$

as the Thouless energy of the junction. Observe that we use $2W$ in the denominator, since that is the distance normal to the interface a quasiparticle travels between successive Andreev reflections [44].

The spectral characteristics of a proximitized system strongly depend on which regime the system is in. Figure 13 shows the dispersion $\epsilon_n(k)$ and density of states ρ per unit length for junctions in the short, intermediate, and long regimes. The density of states is given by

$$\begin{aligned} \rho(E) &= \frac{1}{2\pi\hbar} \sum_n \int \delta[E - \epsilon_n(k)] \frac{dE}{|v(E)|} \\ &= \frac{1}{2\pi\hbar} \sum_n \left| \frac{d\epsilon_n(k)}{dk} \right|^{-1}. \end{aligned} \quad (\text{A2})$$

Here, n is the subband index including spin and we have used $\hbar v = dE/dk$ for the velocity v . In the left-hand column, the solid lines give the dispersion of the hybrid structure, while the dotted lines show the electron and hole dispersions of the normal channel only (with $W_{sc} = 0$ or $\gamma = 0$). In all cases, $\mu \gg \Delta$, and ρ has been broadened by convolution with a Lorentzian of full width at half maximum $\Gamma \ll \Delta$. For the short junction, we indeed have $\Delta_{ind} \approx \Delta$, which manifests as an essentially hard superconducting gap for $|E| < \Delta_{ind}$. We have verified that ρ vanishes identically in this regime with $\Gamma \rightarrow 0$. In the intermediate and long regimes, subgap states exist at energies smaller than Δ , which manifests as a nonzero subgap ρ (soft gap). The difference between the two regimes is the number of these states: in an intermediate junction they are few, but they are multiple in the long-junction limit, as the conditions $\Delta \gtrsim E_{Th}$ and $\Delta \gg E_{Th}$ indicate. Observe that in both cases the subgap bands are flat around $k = 0$

and drop towards a minimum in energy as k increases before rising sharply again [67]. Superimposed on this are intraband oscillations that happen on a smaller energy scale. In principle, oscillations thus manifest in ρ on two energy scales: the larger energy scale is the interband spacing around $k = 0$ ($\propto 1/W^2$), and the smaller the scale of intraband oscillations. Overall, the former has a larger contribution to ρ due to the small curvature in the dispersion. Oscillations on both scales are clearly visible for the intermediate junction. However, increasing Γ further (dashed curve) washes out the fine structure due to intraband oscillations. As a result, ρ gradually increases towards a maximum, when E aligns with the energy of the subgap state around $k = 0$. On the other hand, in the long junction there are multiple states at subgap energies, and the most prominent feature in ρ is the peaks associated with the flat parts of those bands. The fine structure due to intraband oscillations is superimposed, but masked by the broadening.

-
- [1] P. G. de Gennes, *Rev. Mod. Phys.* **36**, 225 (1964).
- [2] G. E. Blonder, M. Tinkham, and T. M. Klapwijk, *Phys. Rev. B* **25**, 4515 (1982).
- [3] T. Tokuyasu, J. A. Sauls, and D. Rainer, *Phys. Rev. B* **38**, 8823 (1988).
- [4] E. A. Demler, G. B. Arnold, and M. R. Beasley, *Phys. Rev. B* **55**, 15174 (1997).
- [5] E. C. Gingrich, B. M. Niedzielski, J. A. Glick, Y. Wang, D. L. Miller, R. Loloee, W. P. Pratt, Jr., and N. O. Birge, *Nat. Phys.* **12**, 564 (2016).
- [6] M. Titov and C. W. J. Beenakker, *Phys. Rev. B* **74**, 041401 (2006).
- [7] H. B. Heersche, P. Jarillo-Herrero, J. B. Oostinga, L. M. K. Vandersypen, and A. F. Morpurgo, *Nature (London)* **446**, 56 (2007).
- [8] V. E. Calado, S. Goswami, G. Nanda, M. Diez, A. R. Akhmerov, K. Watanabe, T. Taniguchi, T. M. Klapwijk, and L. M. K. Vandersypen, *Nat. Nanotechnol.* **10**, 761 (2015).
- [9] J. Alicea, *Rep. Prog. Phys.* **75**, 076501 (2012).
- [10] M. Leijnse and K. Flensberg, *Semicond. Sci. Technol.* **27**, 124003 (2012).
- [11] C. Beenakker, *Annu. Rev. Condens. Matter Phys.* **4**, 113 (2013).
- [12] S. B. Bravyi and A. Y. Kitaev, *Ann. Phys.* **298**, 210 (2002).
- [13] V. Mourik, K. Zuo, S. M. Frolov, S. R. Plissard, E. P. A. M. Bakkers, and L. P. Kouwenhoven, *Science* **336**, 1003 (2012).
- [14] A. Das, Y. Ronen, Y. Most, Y. Oreg, M. Heiblum, and H. Shtrikman, *Nat. Phys.* **8**, 887 (2012).
- [15] M. T. Deng, C. L. Yu, G. Y. Huang, M. Larsson, P. Caroff, and H. Q. Xu, *Nano Lett.* **12**, 6414 (2012).
- [16] T. M. Klapwijk, *J. Supercond.* **17**, 593 (2004).
- [17] S. Guéron, H. Pothier, N. O. Birge, D. Esteve, and M. H. Devoret, *Phys. Rev. Lett.* **77**, 3025 (1996).
- [18] D. I. Pikulin and Y. V. Nazarov, *JETP Lett.* **94**, 693 (2012).
- [19] G. Kells, D. Meidan, and P. W. Brouwer, *Phys. Rev. B* **86**, 100503 (2012).
- [20] S. Mi, D. I. Pikulin, M. Marciani, and C. W. J. Beenakker, *J. Exp. Theor. Phys.* **119**, 1018 (2014).
- [21] E. Prada, P. San-Jose, and R. Aguado, *Phys. Rev. B* **86**, 180503 (2012).
- [22] C. Moore, T. D. Stanescu, and S. Tewari, [arXiv:1611.07058](https://arxiv.org/abs/1611.07058).
- [23] C.-X. Liu, J. D. Sau, T. D. Stanescu, and S. D. Sarma, *Phys. Rev. B* **96**, 075161 (2017).
- [24] J. M. Byers and M. E. Flatté, *Phys. Rev. Lett.* **74**, 306 (1995).
- [25] S. Russo, M. Kroug, T. M. Klapwijk, and A. F. Morpurgo, *Phys. Rev. Lett.* **95**, 027002 (2005).
- [26] R. W. Reithaler, P. Recher, and E. M. Hankiewicz, *Phys. Rev. Lett.* **110**, 226802 (2013).
- [27] G. Falci, D. Feinberg, and F. W. J. Hekking, *Europhys. Lett.* **54**, 255 (2001).
- [28] R. Mélin and D. Feinberg, *Eur. Phys. J. B* **26**, 101 (2002).
- [29] D. Beckmann, H. B. Weber, and H. v. Löhneysen, *Phys. Rev. Lett.* **93**, 197003 (2004).
- [30] J. Brauer, F. Hübner, M. Smetanin, D. Beckmann, and H. v. Löhneysen, *Phys. Rev. B* **81**, 024515 (2010).
- [31] J. Schindele, A. Baumgartner, R. Maurand, M. Weiss, and C. Schönenberger, *Phys. Rev. B* **89**, 045422 (2014).
- [32] P. Recher, E. V. Sukhorukov, and D. Loss, *Phys. Rev. B* **63**, 165314 (2001).
- [33] J. P. Morten, A. Brataas, and W. Belzig, *Phys. Rev. B* **74**, 214510 (2006).
- [34] H. Haugen, D. Huertas-Hernando, A. Brataas, and X. Waintal, *Phys. Rev. B* **81**, 174523 (2010).
- [35] F. Crépin, P. Burset, and B. Trauzettel, *Phys. Rev. B* **92**, 100507 (2015).
- [36] Y.-T. Zhang, Z. Hou, X. C. Xie, and Q.-F. Sun, *Phys. Rev. B* **95**, 245433 (2017).
- [37] J. Liu, J. Song, Q.-F. Sun, and X. C. Xie, *Phys. Rev. B* **96**, 195307 (2017).
- [38] G. Deutscher and D. Feinberg, *Appl. Phys. Lett.* **76**, 487 (2000).
- [39] L. Hofstetter, S. Csonka, J. Nygard, and C. Schönenberger, *Nature (London)* **461**, 960 (2009).
- [40] L. G. Herrmann, F. Portier, P. Roche, A. L. Yeyati, T. Kontos, and C. Strunk, *Phys. Rev. Lett.* **104**, 026801 (2010).
- [41] A. R. Akhmerov, J. P. Dahlhaus, F. Hassler, M. Wimmer, and C. W. J. Beenakker, *Phys. Rev. Lett.* **106**, 057001 (2011).
- [42] B. M. Fregoso, A. M. Lobos, and S. D. Sarma, *Phys. Rev. B* **88**, 180507 (2013).
- [43] P. Szumniak, D. Chevallier, D. Loss, and J. Klinovaja, *Phys. Rev. B* **96**, 041401 (2017).
- [44] D. Sticlet, B. Nijholt, and A. Akhmerov, *Phys. Rev. B* **95**, 115421 (2017).

- [45] M. Kjaergaard, F. Nichele, H. J. Suominen, M. P. Nowak, M. Wimmer, A. R. Akhmerov, J. A. Folk, K. Flensberg, J. Shabani, C. J. Palmstrøm, and C. M. Marcus, *Nat. Commun.* **7**, 12841 (2016).
- [46] H. Zhang, Ö. Gül, S. Conesa-Boj, M. Nowak, M. Wimmer, K. Zuo, V. Mourik, F. K. de Vries, J. van Veen, M. W. A. de Moor, J. D. S. Bommer, D. J. van Woerkom, D. Car, S. R. Plissard, E. P. A. M. Bakkers, M. Quintero-Pérez, M. C. Cassidy, S. Koelling, S. Goswami, K. Watanabe, T. Taniguchi, and L. P. Kouwenhoven, *Nat. Commun.* **8**, 16025 (2017).
- [47] M. P. Anantram and S. Datta, *Phys. Rev. B* **53**, 16390 (1996).
- [48] C. W. Groth, M. Wimmer, A. R. Akhmerov, and X. Waintal, *New J. Phys.* **16**, 063065 (2014).
- [49] See Supplemental Material at <http://link.aps.org/supplemental/10.1103/PhysRevB.97.045421> for the source code that produces the data and figures.
- [50] T. O. Rosdahl, A. Vuik, M. Kjaergaard, and A. R. Akhmerov, TU Delft. Dataset. (2017), doi:10.4121/uuid:5f49027a-5213-4615-94f8-b8026ce795a3.
- [51] B. Nijholt and A. R. Akhmerov, *Phys. Rev. B* **93**, 235434 (2016).
- [52] All parameters are provided per figure in a text file as Supplemental Material [49].
- [53] T. Ando, *Phys. Rev. B* **44**, 8017 (1991).
- [54] M. Hell, M. Leijnse, and K. Flensberg, *Phys. Rev. Lett.* **118**, 107701 (2017).
- [55] F. Pientka, A. Keselman, E. Berg, A. Yacoby, A. Stern, and B. I. Halperin, *Phys. Rev. X* **7**, 021032 (2017).
- [56] B. J. Wieder, F. Zhang, and C. L. Kane, *Phys. Rev. B* **89**, 075106 (2014).
- [57] D. Feinberg, *Eur. Phys. J. B* **36**, 419 (2003).
- [58] I. C. Fulga, F. Hassler, A. R. Akhmerov, and C. W. J. Beenakker, *Phys. Rev. B* **83**, 155429 (2011).
- [59] J. J. He, J. Wu, T.-P. Choy, X.-J. Liu, Y. Tanaka, and K. T. Law, *Nat. Commun.* **5**, 3232 (2014).
- [60] W. Chen, D. N. Shi, and D. Y. Xing, *Sci. Rep.* **5**, 7607 (2015).
- [61] D. Aasen, S.-P. Lee, T. Karzig, and J. Alicea, *Phys. Rev. B* **94**, 165113 (2016).
- [62] C. W. J. Beenakker, in *Transport Phenomena in Mesoscopic Systems: Proceedings of the 14th Taniguchi Symposium, Shima, Japan, November 10–14, 1991*, edited by H. Fukuyama and T. Ando (Springer, Berlin, 1992), Chap. 3, pp. 235–253.
- [63] A. Volkov, P. Magnée, B. van Wees, and T. Klapwijk, *Physica C (Amsterdam, Neth.)* **242**, 261 (1995).
- [64] S. Pilgram, W. Belzig, and C. Bruder, *Phys. Rev. B* **62**, 12462 (2000).
- [65] G. Tkachov, *Physica C (Amsterdam, Neth.)* **417**, 127 (2005).
- [66] C. R. Reeg and D. L. Maslov, *Phys. Rev. B* **94**, 020501 (2016).
- [67] M. Titov, A. Ossipov, and C. W. J. Beenakker, *Phys. Rev. B* **75**, 045417 (2007).